

# Demonstrating sub-nm closed loop MEMS flattening

Julia W. Evans\*, Bruce Macintosh, Lisa Poyneer

Lawrence Livermore National Laboratory  
7000 East Ave, Livermore, CA 94550

Katie Morzinski, Scott Severson, Daren Dillon, Donald Gavel, Layra  
Reza

UCO Lick Observatory, Laboratory for Adaptive Optics, University of California at Santa  
Cruz

1156 High St., Santa Cruz, CA, 95064

[evans74@llnl.gov](mailto:evans74@llnl.gov)

**Abstract:** Ground based high-contrast imaging (e.g. extrasolar giant planet detection) has demanding wavefront control requirements two orders of magnitude more precise than standard adaptive optics systems. We demonstrate that these requirements can be achieved with a 1024-Micro-Electrical-Mechanical-Systems (MEMS) deformable mirror having an actuator spacing of  $340\ \mu\text{m}$  and a stroke of approximately  $1\ \mu\text{m}$ , over an active aperture 27 actuators across. We have flattened the mirror to a residual wavefront error of 0.54 nm rms within the range of controllable spatial frequencies. Individual contributors to final wavefront quality, such as voltage response and uniformity, have been identified and characterized.

© 2006 Optical Society of America

**OCIS codes:** (010.1080) adaptive optics, (230.3990) microstructure devices, (350.1260) astronomical optics

---

## References and links

1. G. W. Marcy, "California and Carnegie Planet Search," U.C. Berkeley (2005). <http://exoplanets.org>.
2. C. H. Lineweaver and D. Grether, "What fraction of sun-like stars have planets?" *Ap. J.* **598**, 1350–1360.
3. A. Burrows, M. Marley, W. B. Hubbard, J. I. Lunine, T. Guillot, D. Saumon, R. Freedman, D. Sudarsky, and C. Sharp, "A nongray theory of extrasolar giant planets and brown dwarfs," *Astrophysical J.* **491**, 856–875 (1997).
4. B. Macintosh, J. Graham, B. Oppenheimer, L. Poyneer, A. Sivaramakrishnan, and J.-P. Veran, "MEMS-based extreme adaptive optics for planet detection," in *MEMS/MOEMS Components and their Applications III*, S. S. Olivier, S. A. Tadiadapa, and A. K. Henning, eds., Proc. SPIE **6113**, pp. 48–57 (2006).
5. A. Sivaramakrishnan, J. P. Lloyd, P. E. Hodge, and B. A. Macintosh, "Speckle decorrelation and dynamic range in speckle noise-limited imaging," *Astrophysical J.* **581**, L59–62 (2002).
6. T. Bifano, P. Bierden, and J. Perreault, "Micromachined Deformable Mirrors for Dynamic Wavefront Control," in *Advanced Wavefront Control: Methods, Devices and Applications II*, J. D. Gonglewski, M. T. Grueneisen, and M. K. Giles, eds., Proc. SPIE **5553**, pp. 1–16 (2004).
7. N. Doble, G. Yoon, L. Chen, P. Bierden, S. Oliver, and D. R. Williams, "Use of a microelectricalmechanical mirror for adaptive optics in the human eye," *Opt. Lett.* **27**, 1537–1539 (2002).
8. K. L. Baker, E. A. Stappaerts, D. Gavel, S. C. Wilks, J. Tucker, D. A. Silva, J. Olsen, S. S. Olivier, P. E. Young, M. W. Kartz, L. M. Flath, P. Krulevitch, J. Crawford, and O. Azucena, "High-speed horizontal-path atmospheric turbulence correction with a large-actuator-number microelectricalmechanical system spatial light modulator in an interferometric phase-conjugation engine," *Opt. Lett.* **29**, 1781–1783 (2004).
9. K. L. Baker, E. A. Stappaerts, D. Gavel, S. C. Wilks, J. Tucker, D. A. Silva, J. Olsen, S. S. Olivier, P. E. Young, M. W. Kartz, L. M. Flath, P. Krulevitch, J. Crawford, and O. Azucena, "Breadboard testing of a phase-conjugate engine with an interferometric wave-front sensor and a microelectricalmechanical systems-based spatial light modulator," *Appl. Opt.* **43**, 5585–5593 (2004).

10. G. Vdovin, P. M. Sarro, and S. Middelhoek, "Technology and applications of micromachined adaptive mirrors," *J. Micromech. Microeng.* **9**, R8–R20.
11. D. Dayton, J. Gonglewski, S. Restaino, J. Martin, J. Phillips, M. Hartman, S. Browne, P. Kervin, J. Snodgrass, N. Heimann, M. Shilko, R. Pohle, B. Carrion, C. Smith, and D. Thiel, "Demonstration of new technology MEMS and liquid crystal adaptive optics on bright astronomical objects and satellites." *Opt. Express* **10**, 1508–1519 (2002).
12. J. Trauger, D. Moody, B. Gordon, Y. Gürsel, M. Ealey, and R. Bagwell, "Performance of a precision high-density deformable mirror for extremely high contrast imaging astronomy from Sapce," in *Future EUV/UV and Visible Space Astrophysics Missions and Instrumentation*, J. C. Blades and O. H. W. Siegmund, eds., Proc. SPIE **4854**, pp. 1–8 (2003).
13. J. W. Evans, G. Sommargren, B. A. Macintosh, S. Severson, and D. Dillon, "Effect of Wavefront Error on  $10^{-7}$  Contrast Measurements," *Opt. Lett.* **31**, 565–567 (2006).
14. G. E. Sommargren, D. W. Phillion, M. A. Johnson, N. Q. Nguyen, A. Barty, F. J. Snell, D. R. Dillon, and L. S. Bradsher, "100-picometer interferometry for EUVL," in *Emerging Lithographic Technologies VI*, R. L. Engelstad, ed., Proc. SPIE **4688**, pp. 316–328 (2002).
15. J. W. Evans, G. Sommargren, L. Poyneer, B. Macintosh, S. Severson, D. Dillon, A. Shenis, D. Palmer, J. Kasdin, and S. Olivier, "Extreme Adaptive Optics Testbed: Results and Future Work," in *Advancements in Adaptive Optics*, D. B. Calia, B. L. Ellerbroek, and R. Ragazzoni, eds., Proc. SPIE **5490**, pp. 954–959 (2004).
16. J. W. Evans, K. Morzinski, L. Reza, S. Severson, L. Poyneer, B. Macintosh, D. Dillon, G. Sommargren, D. Palmer, D. Gavel, and S. Olivier, "Extreme Adaptive Optics Testbed: High Contrast Measurements with a MEMS Deformable Mirror," in *Techniques and Instrumentation for Detection of Exoplanets II*, D. R. Coulter, ed., Proc. SPIE **5905**, pp. 303–310 (2005).
17. J. W. Evans, K. Morzinski, S. Severson, L. Poyneer, B. Macintosh, D. Dillon, L. Reza, D. Gavel, D. Palmer, S. Olivier, and P. Birden, "Extreme Adaptive Optics Testbed: Performance and Characterization of a 1024-MEMS deformable mirror," in *MEMS/MOEMS Components and their applications III*, S. Olivier, ed., Proc. SPIE **6113**, pp. 131–136 (2006).
18. L. A. Poyneer and B. Macintosh, "Experimental demonstration of phase correction with a 32 x 32 microelectromechanical systems mirror and a spatially filtered wavefront sensor," *J. Opt. Soc. Am. A* **21**, 810–819 (2004).
19. H. R. Shea, A. Gasparyan, C. D. White, R. B. Comizzoli, D. Abushch-Magder, and S. Arney, "Anodic Oxidation and Reliability of MEMS Poly-Silicon Electrodes at High Relative Humidity and High Voltages," in *MEMS Reliability for Critical Applications*, R. A. Lawton, ed., Proc. SPIE **4180**, pp. 117–122 (2000).
20. F. Malbet, J. Yu, and M. Shao, "High Dynamic Range Imaging Using a Deformable Mirror for Space Coronagraphy," *Publications Of The Astronomical Society of the Pacific* **107**, 386–398 (1995).
21. L. A. Poyneer, B. Bauman, B. A. Macintosh, D. Dillon, and S. Severson, "Spatially filtered wave-front sensor for high-order adaptive optics," *Opt. Lett.* **31**, 293–295 (2006).

## 1. Introduction

The detection of over 150 extrasolar planets [1] has placed planetary science at the forefront of astronomy. Most of these detections were made with radial velocity techniques, which measure the doppler shift of the parent star produced by the gravitational pull of a planet. These techniques only probe about 15% of the orbital parameter space of our solar system [2] meaning that planets of the size and position of our own solar system are largely unobserved by current research. Imaging extrasolar planets would open a large complimentary region to radial velocity techniques and a survey of this kind would provide valuable information about the distribution of planets in a 'typical' system. Imaging can also provide additional information about planets. For example, spectroscopic data could be used to investigate the material composition of exoplanets. Several observatories including the Gemini Observatory and the Very Large Telescope have recognized extrasolar planet imaging as a key science goal and funded ground-based planet imagers to meet that need. These ground based systems will require a specialized form of adaptive optics (AO) known as Extreme Adaptive Optics (ExAO) to achieve the high-contrast images needed to image extrasolar planets. The work presented here was undertaken in support of the Gemini Planet Imager (GPI).

Ground based extrasolar planet imagers will look for young Jupiter-like planets that are still glowing with the heat of formation. This type of imaging will require contrasts of between  $10^{-6}$  and  $10^{-7}$  [3], making these instruments technically challenging. Stringent requirements for the number of actuators, precision of flattening and frame rate make deformable mirror

(DM) technology a particular risk area. GPI will require approximately 2000 actuators [4], for a clear aperture of 44 actuators across. Even one non-working actuator cannot be tolerated in the aperture because it will scatter light into the discovery region. Contrast is ultimately limited by residual static wavefront errors [5], so GPI will require wavefront control with an accuracy of better than 1 nm rms within the low- to mid-spatial frequency range [4]. Space-based planet detection architectures have similar requirements. The first step to demonstrating this is to flatten the mirror itself — in the absence of aberrations — to the  $< 1$  nm level. An extrasolar planet imager will need to correct additional aberrations, but tests without aberration identify performance limits for future more realistic tests and also demonstrate the internal calibration requirements for the DM in an ExAO system. To adequately correct the changing atmosphere the system must run at 2500 Hz [4]. Stroke requirements are reduced by the combination of two DMs. A large-stroke deformable mirror will be used for large low-order wavefront correction (woofer) and a high-order device will be used for smaller mid- to high-order correction (tweeter). A traditional deformable mirror to meet the high actuator count requirement would be prohibitively large and expensive (\$1000/channel).

Micro-Electrical-Mechanical-Systems (MEMS) deformable mirrors, such as those manufactured by Boston Micromachine Corporation (BMC) [6], are a promising solution to the DM problem. MEMS are fabricated of polysilicon and utilize an array of independently addressable electrostatic actuators. The device discussed here has an actuator spacing of  $340 \mu\text{m}$  making it about 10 mm across. The device is specified by BMC to have  $2 \mu\text{m}$  of stroke, although with our current operating parameters we have about  $1 \mu\text{m}$ . The top surface of the DM is a continuous gold-coated mirror which can be deformed by the actuators underneath. Performance testing and device characterization are ongoing at the Laboratory for Adaptive Optics (LAO) at University of California, Santa Cruz. We have focused on the precision flattening requirement using a 1024 actuator device (the largest device currently available) and the results are presented in this paper.

MEMS deformable mirrors have been used successfully in other AO systems. In a vision science system, Doble *et al.* [7] compared the performance of a 144 segmented MEMS device to a more traditional Xinetics DM. They found the MEMS DM to have comparable performance except when the MEMS DM was limited by stroke. A 1024 segmented device was tested in a horizontal path application at frame rates in excess of 800 Hz with strehl ratios  $> 0.5$  by Baker *et al.* [8]. Testbed work was also done with the segmented device using Kolmogorov phase screens to introduce aberrations [9]. A major limitation of this earlier segmented MEMS device was the number of inactive actuators.

A similar DM technology is membrane electrostatic deformable mirrors. Much development work and testing has gone into these devices [10], including some on-sky tests [11]. Typically these devices have fewer actuators and much broader, modal influence functions than their MEMS counterparts. Membrane mirrors are more suited to curvature systems than high contrast systems, which need to fit well-defined fourier modes.

A modular electroceramic deformable mirror developed by Xinetics and tested by the Jet Propulsion Laboratory (JPL) is another possibility for a large actuator count deformable mirror. There are versions with 1024 and 4096 actuators. The 1024 version has been tested extensively in the High Contrast Imaging Testbed at JPL [12], where it is kept in a temperature controlled vacuum chamber. JPL has achieved angstrom level flatness within controllable spatial frequencies and stability has been demonstrated to 0.01 angstrom [12]. The 500-nm stroke and mm-pitch make it a challenging device for use in ground based astronomical systems. Smaller optics are advantageous in high-contrast systems because of improved optical quality compared to larger optics.

The ExAO testbed is uniquely suited to testing MEMS deformable mirrors in the high-

contrast regime. We have already demonstrated an ability to operate at contrast levels of  $10^{-7}$  to  $10^{-8}$  [13]. The extremely accurate optical metrology of the phase shifting diffraction interferometer (PSDI) [14] allows absolute measurements of the MEMS DM. Using the PSDI as the wavefront sensor we have flattened to  $< 1$  nm rms over controllable spatial frequencies. The technical challenges in achieving this result can be broken into three categories: measuring the phase, controlling the MEMS, and the stability of the system. Errors in each of these tasks leads to errors in flattening performance and are summarized in an error budget. Preliminary work with the MEMS device, including some of the engineering challenges leading up to this result, have been presented in prior works [15, 16, 17]. A complete inventory of these difficulties and our mitigation techniques are included here.

## 2. Description of ExAO testbed

The testbed has two modes of operation: imaging mode and interferometry mode. In imaging mode contrast can be measured directly, while in interferometer mode wavefront phase is measured. (Wavefront mode is shown in Fig. 1). Contrast is directly related to wavefront error (WFE) and wavefront measurements are used to simulate image data. The comparison provides an internal consistency check for all measurements. The testbed was designed for operation in the high-contrast regime thus it has low WFE without active correction, an enclosure to reduce air turbulence and baffling to prevent scattered light. In initial experiments without active correction we demonstrated the total WFE of the testbed is 1.5 nm RMS with about 1 nm of that falling within the range of controllable spatial frequencies of our MEMS DMs [13]. In imaging mode the reference pinhole is replaced with a CCD camera and only the probe beam is used. Further information about contrast measurements can be found in prior works [13, 16].

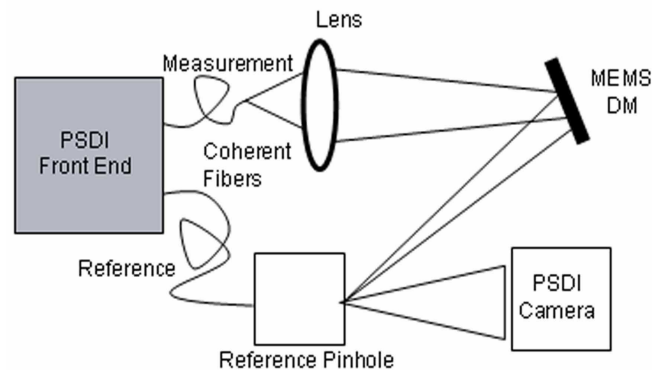


Fig. 1. Simplified schematic of interferometry mode on the ExAO testbed. A physical aperture can be placed in front of the MEMS but during closed loop operation a software aperture is used.

In interferometry mode, the testbed becomes an extremely accurate optical metrology system. The PSDI was developed at Lawrence Livermore National Laboratory for metrology of aspheric optics for use at UV wavelengths [14]. (In its original layout the PSDI has an absolute wavefront accuracy of 100 pm. In the experiment described here we estimate accuracy to be better than 250 pm.) A probe (or measurement) wavefront is injected from the upper single-mode fiber in Fig. 1. This passes through the system and is focused onto a pinhole embedded in a super-polished flat mirror (the reference pinhole). Meanwhile, a coherent reference beam

passes through the pinhole and interferes with the outgoing probe wavefront. The interference pattern is recorded at a CCD located in an arbitrary location along the optical axis. Using standard phase-shifting interferometer techniques this produces a measurement of the fringe pattern at this location, which can then be converted to a wavefront. This wavefront is numerically propagated in two steps to the plane of interest using the ABCD matrix and a Huygens Integral transformation implemented with FFTs [14].

Wavefront measurements are used to control the MEMS during closed loop operations. The spatial resolution at the MEMS plane is limited by truncation effects due to an aperture at the reference pinhole. The effective resolution in the MEMS plane is  $\sim 141 \mu\text{m}$  or 41% of an actuator. For closed loop operation, programs in the interactive data language (IDL) are used to direct data acquisition (wavefront sensing with the PSDI), back propagation calculations and commanding the MEMS device through the MEMS driver. Before closed loop operation, the alignment and voltage response of the system must be calibrated. Alignment is done by activating four known actuators on the MEMS and noting their position in a wavefront measurement. For voltage calibration the response of each actuator is measured and fit with a quadratic. These calibration measurements are used to convert wavefront measurements into actuator by actuator phase and then to the corresponding voltages. Closed loop operations can also be run with a spatially filtered Shack-Hartman wavefront sensor [18].

### 3. MEMS deformable mirrors

We have tested a total of ten 1024-actuator deformable MEMS mirrors fabricated by Boston Micromachines Corporation [6]. While a future exoplanet imager will require more actuators, the 1024 device is the largest commercially available MEMS device. Characterization and performance testing of these devices have provided feedback to the design and specification of the larger device. We have characterized voltage response, actuator uniformity and device stability as these characteristics will affect closed loop performance.

MEMS DMs are fabricated using bulk processing techniques, meaning that many are produced at once. We have tested mirrors from several such fabricating runs. Surface micromachining processes are used to fabricate the mirrors and the structures on them are made of polysilicon [6]. Each individually addressable actuator is composed of two electrodes which when activated are attracted due to the voltage potential. The top electrode of each actuator is held in place by a combination of springs which provide the restoring force. More complete information about the BMC mirror can be found in Bifano *et al.* [6]. MEMS DM technology for ExAO applications are still under development but over these ten devices we have seen a dramatic improvement in unpowered flatness and yield which will be crucial for the 4000 actuator device. The 1024 mirrors have 4 inactive actuators by design (they are wired to ground). The actuators are spaced  $340 \mu\text{m}$  apart with a continuous face sheet as the top surface. Due to residual manufacturing stress the top surfaces of these devices have curvature. Early devices had  $> 200 \text{ nm rms}$  unpowered WFE, but more recent devices have had as little as  $50 \text{ nm rms}$  unpowered WFE.

In general defective actuators occur during the manufacturing process rather than failing during operation. However, a combination of high humidity and high voltage can produce oxidation in individual actuators which will eventually limit the performance of those actuators [19]. To avoid humidity damage the device can be sealed under a glass window, or only operated in a controlled laboratory environment. An unpowered device is not damaged by high humidity (but if condensation occurs the mirror must be dry before it is activated). Two of the devices tested, including the device with the best closed loop performance, have windows. ‘Snap-down’ can also damage actuators. This occurs when an actuator has too much displacement and the electrical attraction compressing the actuator overcomes the mechanical force that allows the actuator

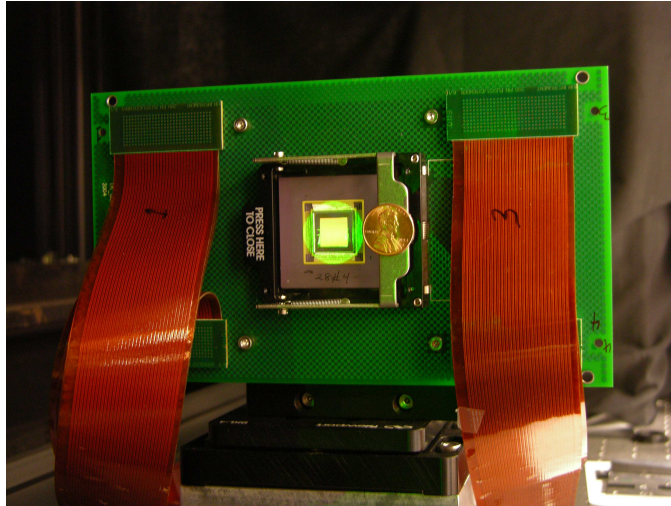


Fig. 2. The 1024 actuator MEMS device made by Boston Micromachines Corporation, shown on the testbed with a penny for scale.

to rebound. These actuators will be stuck in the maximum displacement position. Two early devices were damaged by humidity at the LAO but no damage due to snap-down has occurred.

The MEMS is controlled with 13-bit D/A conversion and amplification using a system developed by Red Nun Electronics Company. The smallest voltage step allowed with these electronics is 0.025 volts for the current configuration. This corresponds to a phase step of 0.18 nm. The driver boards for many-channel systems like this are also under development. It is critical and tedious to ensure that the mapping through the driver electronics is accurate. Minor damage to the boards can be difficult to detect and will negatively affect closed loop performance.

### 3.1. Voltage response

One limitation of MEMS DM technology is the device's limited stroke, especially compared with macro-DM technology. In practice, we find that MEMS stroke depends on the position of neighboring actuators as expected for their relatively broad influence functions, which have approximately 26% crosstalk. Two actuators away the crosstalk reduces to 4%. A 3 by 3 array of actuators will have more displacement at a given voltage than a single actuator at the same voltage. In Fig. 3 this difference is indicated by the 3 dotted versus solid lines. In a typical AO system the DM is operated at a bias to correct both positive and negative wavefront errors. The entire device is set at an intermediate voltage and actuators are moved by varying their voltage about the bias. We typically operate at a bias of 110 volts, that voltage being midway in our operational displacement. We set a maximum voltage limit to 160 volts to prevent snap-down both in software and on the voltage power supply. An imbalance between the electrostatic force of activating an actuator and the mechanical restoring force causes stroke at a bias to be reduced. Figure 3 summarizes the results of testing the stroke of a particular MEMS device for these situations. For this test 4 actuators were activated at several incremental voltages and their displacement relative to the flat surface of the MEMS were measured with a Zygo interferometer. The test was also done with a set of adjacent actuators moved in a 3 by 3 box. Both tests were done with a bias voltage of 0, 110 and 160 volts. In Fig. 3 the resultant curves have been re-centered so that 0 displacement is at 0 volts rather than at the bias voltage. In typical operations these devices achieve about 1  $\mu\text{m}$  of stroke with our operational parameters,

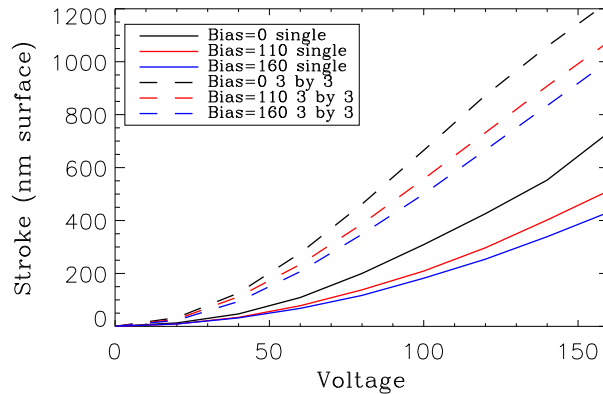


Fig. 3. Stroke of a device measured with 0, 110, and 160 volt bias for an individual or group of actuators. More stroke is achieved when actuators move together without a bias voltage.

similar to the measured response of the 3 by 3 array because actuators are not significantly displaced from their neighbors during closed loop. The ‘snap-down’ effect is caused by too much displacement, not too much voltage. There is potential to increase the stroke of the device by increasing operational voltage above the current 160 volt maximum, while within the range of acceptable displacement. Because additional stroke was not required for our tests, increasing maximum voltage was not investigated.

MEMS actuators have a non-linear response to voltage that varies on a individual device and between devices. We calibrate the voltage response of every actuator on a device. In this test one actuator in each 4 by 4 array of actuators on the device is tested at varying voltages cyclically until all of the actuators are tested. There are 16 frames for each voltage level, with 64 actuators tested in each frame. A few actuators have a particularly irregular response which can be an issue for closed loop high-contrast operation. These irregular actuators are discussed in greater detail in the next section. In early tests the average voltage response of four actuators was used to calibrate the entire device. Performance was improved, particularly for irregular actuators, by calibrating individual responses.

### 3.2. Actuator uniformity

Operating in closed loop mitigates the effect of small variations in voltage response between actuators. On the most recent device the variation in maximum displacement at 160 volts is less than 5% (excluding the outer two rows and columns of actuators), which is well within our ability to flatten. Irregular actuators, however, are unable to achieve the desired position, regardless of number of iterations, producing an in-band fitting error that limits closed loop performance. We have identified three categories of such actuators: no-response (or dead), low-response and coupled. Typically we refer to the yield of a MEMS device as percentage of working actuators. This number is particularly important in high-contrast applications as no-response actuators scatter light into the region of interest. Actuator uniformity refers to the variability of all ‘working’ actuators including low-response and coupled actuators.

Figure 4 is a representation of actuator yield and uniformity in three tested devices. No-response actuators are marked in red, other irregular actuators in yellow and normal actuators are white. The three figures exclude the outer 2 rows and columns which are outside the aperture and difficult to characterize. The left device was received in Nov 2004. It had limited

performance due to the number of irregular actuators and was operated over a smaller aperture because of the number and placement of no-response actuators. The middle and right devices were received in Feb and Oct of 2005. The two no-response actuators in the top middle of all three devices are wired to ground and are excluded from the following statistics. The oldest device has 96.9 % normal actuators (33 irregular) while the most recent device has 99.5% normal actuators (5 irregular). Only 94.1 % of actuators were normal (60 irregular) in tests of the segmented device published by Baker et. al. in 2004 [9, 8]. This dramatic improvement in actuator yield and uniformity has allowed improved performance and made MEMS deformable mirrors a feasible technology for high-contrast applications.

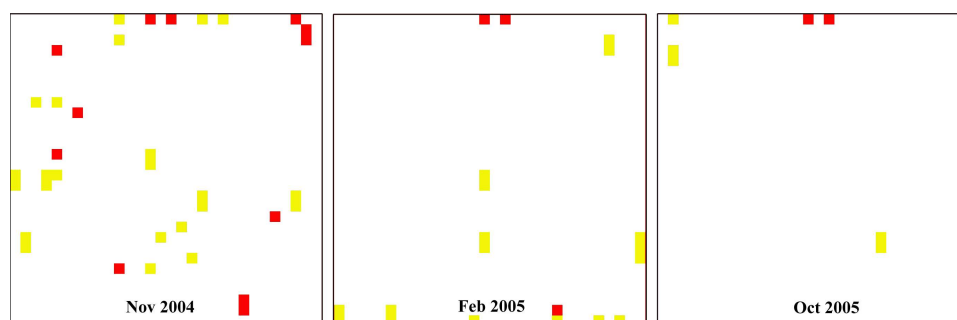


Fig. 4. Irregular actuators are identified for the working region of three MEMS devices. Red indicates a no-response actuator, yellow a ‘working’ irregular actuator, and white is a normal actuator. The Nov 2004 device had limited performance due to the number of irregular actuators and was operated over a smaller aperture because of the number and placement of no-response actuators. There has been a dramatic improvement in both yield and uniformity in the Feb and Oct 2005 devices. The two no-response actuators in the top middle of all three devices are wired to ground.

With fewer no-response actuators the effects of other irregular actuators have become more apparent. Careful characterization of irregular actuators has lead to improved control and provided engineering feedback to the manufacturer. As mentioned above we have categorized irregular actuators as low-response, or coupled. Low-response actuators can be actuators that only move with their neighbors or actuators with reduced voltage response. The Feb 2005 device in Fig. 4 has a low-response actuator that only moves with its neighbors, right in the center. After flattening, this actuator is offset from its neighbors by about 20 nm. In previous tests with this device [16], more irregular actuators were apparent due to errors in the driver electronics, but this electronics problem has since been corrected. Coupled actuators affect voltage calibration. For example in our best performing device (Oct 2005) there are two coupled actuators. When a coupled actuator’s voltage response is tested individually there is no displacement after the bias voltage, because the other actuator in the pair is set to the bias during the test. If coupled actuators are tested simultaneously the voltage response is normal. (See Fig. 5.) A coupled actuator will move to the lesser of the voltage applied to the pair.

### 3.3. Stability

Current closed loop tests use the PSDI as the wavefront sensor, which limits frame rate. As a result, excellent stability for both the system and the MEMS is required. To test MEMS stability, a flattened shape is applied to the MEMS device and successive wavefront measurements are taken every 38 seconds (the minimum time to complete a PSDI measurement) for 60 iterations. Short term stability is measured over 9 minute intervals within the long term stability test. The

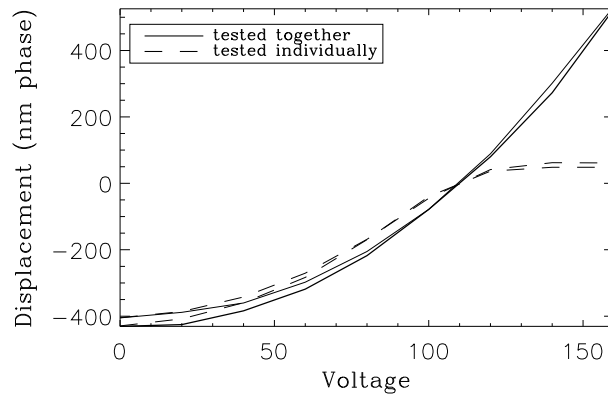


Fig. 5. Voltage response of two coupled actuators tested individually and together, with a bias voltage of 110 volts.

shorter time scale is comparable to typical closed loop operation times. The variation of each actuator in phase from its initial position is calculated with piston and tip/tilt removed. This analysis was done over approximately half of the device. The PSDI stability was measured to be 0.08 nm rms phase by replacing the MEMS with a flat mirror. The average long term stability of the MEMS was measured as 0.16 nm rms phase. On the shorter time scale the system is more stable with an average RMS deviation of 0.13 nm rms phase for the MEMS and 0.07 nm rms phase for the flat mirror. Previous tests had indicated less stability [16] because of errors produced by the MEMS drive electronics that have since been corrected. Figure 6 is a curve of growth showing that most of the actuators are quite stable. Of the 500 tested 97% are stable to better than 0.16 nm rms surface over 38 minutes.

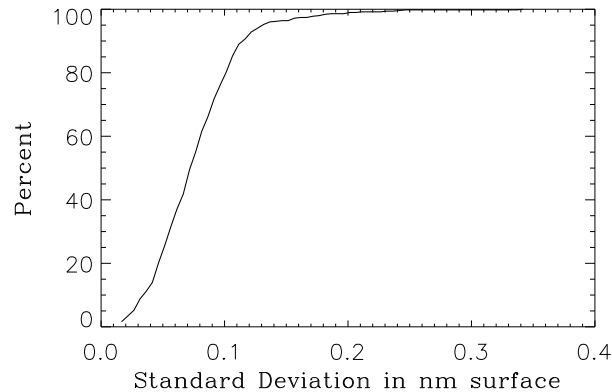


Fig. 6. Curve of growth for stability data. Of the 500 actuators tested 97% stability of better than 0.16 nm (standard deviation of surface over 60 measurements taken in 38 minutes).

#### 4. Closed loop performance

In these closed loop tests no additional aberrations were introduced into the system. The primary source of error is the MEMS DM itself. Although a ground based extrasolar planet imager will have to correct the atmosphere the more basic test here identifies the performance limitations of future more realistic tests. A planet imager will also have a stringent internal calibration requirement of  $<1$  nm (in mid-spatial frequencies). These experiments demonstrate we can meet that requirement. The metric we use for closed loop performance is wavefront error within the range of spatial frequencies which the DM can correct. Higher spatial frequencies will scatter to larger angles [5]. Using a numerical spatial filter to avoid aliasing a dark hole region over controllable spatial frequencies will be created in the far field image (or the power spectrum of the wavefront) [20, 21](See Fig. 9). There are some higher order effects which cause higher order aberrations to fold into the dark hole, but these are small especially in a case with no additional aberration, making in-band wavefront error a good metric for a high-contrast system.

The ExAO testbed was designed to minimize measurement and stability errors so that closed loop operation would be primarily a test of MEMS performance. In previous closed loop tests

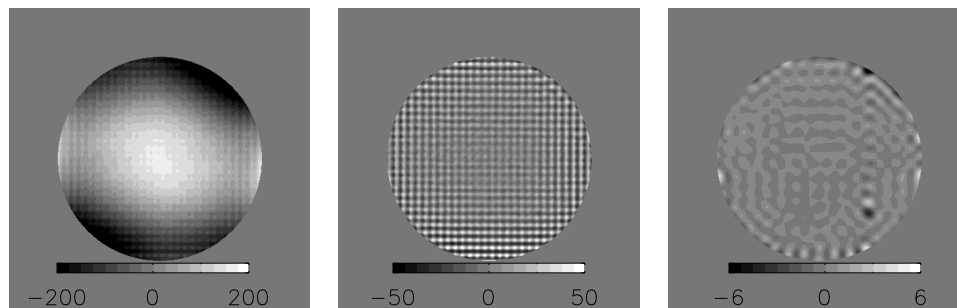


Fig. 7. Wavefronts taken before and after a closed loop test with a 9.2 mm aperture. The initial wavefront has an RMS WFE of 148 nm, while the flattened wavefront has 12.8 nm total RMS wavefront error, which is mostly errors on the scale of an individual actuator. Inside the controlled range of spatial frequencies the rms wavefront error is 0.54 nm. This is seen more clearly in the lowpass filtered image (far right).

a 10-mm circular aperture was placed slightly in front of the MEMS device during flattening. In the most recent tests the physical aperture was replaced with a software aperture of the same size (9.2 mm in the MEMS plane) to reduce diffraction from the edge of the physical mask. A ring two actuators wide around the outside of the aperture is slaved to the final ring of actuators inside the aperture using a nearest neighbor average because a discontinuity between controlled and uncontrolled actuators can produce a ringing ‘edge’ effect during closed loop. Typically the closed loop is run for between 16-25 iterations, and most of the correction takes place within the first five iterations. The test shown in Fig. 7 was run for 25 iterations with the best flattening occurring at iteration 20. Tip/Tilt is not actively controlled. After a device is partially flattened tip/tilt is removed optically. After that, flattening is done with tip/tilt removed numerically. Before running closed loop the wavefront had 148.1 nm total rms WFE, and after flattening the wavefront had 12.8 nm total rms WFE and only 0.54 nm rms WFE inside the controlled range of spatial frequencies. This level of performance of the system is quite repeatable. Out-of-band error is dominated by print through, however this particular device has similar amounts of print through and almost twice as much out-of-band WFE than the Feb. 2004 device. Perhaps the additional error is caused by the window. The wavefront improvement is noticeable in Fig. 7.

The large structure of the errors in the initial wavefront have been corrected in the final wavefront (middle image), revealing smaller structures on the scale of an individual actuator. Those small-structure errors fall outside of the region of controllable errors. By filtering out those high-spatial-frequency errors the limitations to closed loop performance can be better investigated (far right image). The light and dark actuators slightly to the right and below center are the coupled actuators discussed previously. They are about 3 nm above and below their neighbors. The effective aperture has a 9.2-mm diameter with approximately 27 actuators across yielding a highest controllable spatial frequency of about 13.5 cycles per aperture and a corresponding control radius in the point spread function of  $13.5\lambda/D$ . The cutoff frequency is apparent in the

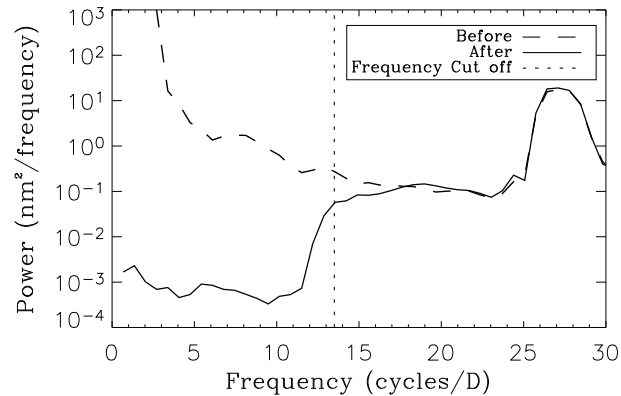


Fig. 8. Power spectrum generated from wavefronts taken before and after flattening. The 27 actuators across the aperture yield a highest controllable spatial frequency of 13.5 cycles per aperture. The bump at 27 cycles per aperture corresponds to physical structures on the MEMS at the scale of the individual actuator spacing.

power spectrum (See Fig. 8) at the edge of the dark hole region. The 27 actuators corresponds to an active aperture covering 84% of the MEMS device. We limit the aperture size to allow for at least 2 rows of slaved actuators around the active aperture, preventing an edge discontinuity which introduces error and to avoid the outer most row/column of the device which is not fully covered by the face sheet and typically has less stroke. Aliasing is prevented with a numerical spatial filtering of the PSDI measurement. A bump in the power spectrum at 27 cycles per aperture indicates the error introduced by print-through of physical structures on the MEMS device at the scale of an individual actuator. The primary affect in the far field of this error will be to produce repeating images of the PSF starting at  $27\lambda/D$ . In high contrast imaging where the region of interest is inside the region of controllable spatial frequencies MEMS print through is not a significant error source (See Fig. 9). The power spectrum was generated with a Blackman window to reduce ringing, and has a slightly reduced total WFE under the curve as a result.

## 5. Limitations to improved performance

Errors in correcting the wavefront can stem from imperfect wavefront measurements, instabilities in the system and the inability of the DM to fit the desired shape. We can summarize these errors in an error budget (See Table 1). We have disregarded errors outside of the controllable spatial frequencies of the MEMS device. Fortunately, those errors will primarily scatter light outside of the region of interest in corresponding far field measurements.

We refer to the largest error source as an edge effect. It is measured by comparing the rms

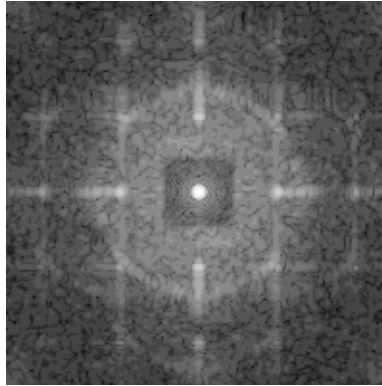


Fig. 9. Far field image simulated from the wavefront measurement shown in Fig.7. Diffraction has been suppressed with a symmetric blackman apodization for illustrating the effect of high spatial frequency errors like print-through on the image.

WFE over the full aperture and over a 75% aperture. In previous results this error source was  $> 1$  nm due to diffraction from the physical aperture and the distance between the aperture and the MEMS device. The physical aperture has been replaced with a software aperture and the edge effect has been reduced to 0.42 nm. Even with this reduction, edge effects remain the largest error source. While diffraction and scattered light from the physical aperture have been removed, other sources remain and introduce error into the PSDI measurements. In particular it is difficult to perfectly baffle light from the uncontrolled edges and wires of the MEMS device. A device window contributes to imperfect baffling. A more advanced optical layout with a well-defined pupil or another type of wavefront sensor could reduce this problem.

The effect of irregular actuators on closed loop performance is clear from the lowpass filtered image (far right of Fig. 7). Devices with more irregular actuators did not flatten as well as this device. The effect of the coupled actuators on flattening was estimated by comparing the rms WFE over 75% of the aperture to the error over the same aperture with the area around the irregular actuators removed. This does not account for any errors caused by the irregular actuators outside of their immediate vicinity. This technique for estimating error does not work well for no-response actuators or many irregular actuators within the aperture.

The remaining errors: voltage, stability and measurement are all system dependent. The voltage step size is determined by the number of bits in the electronics split over the voltage range, currently 0 to 200 volts. This voltage step size is converted to phase using a typical voltage response in the vicinity of the bias voltage. The response over the small region required to correct most of the device is quite linear, but if more stroke on the device were required this error could become larger. Voltage step size could be reduced with higher resolution drivers, or a change in the voltage range. The stability of the device was discussed previously. Measurement error is inherent to the PSDI system and is calculated by comparing two measurements taken consecutively. Alignment errors of the input fiber of the PSDI measurement leg increase measurement error.

The calculated wavefront error agrees well with the measured WFE indicating that these errors are the limiting errors for improved performance.

## 6. Conclusion

Our testing has demonstrated that MEMS deformable mirrors can be controlled at the level of precision needed for high-contrast AO systems. We have flattened a MEMS deformable mirror

Table 1. Error budget for best flattening result over a 9.2 mm aperture within controllable spatial frequencies. The experimental residual WFE is 0.54 nm rms within controllable spatial frequencies and corresponds well to the error budget.

Error Source	nm RMS
Edge Effects	0.42
Irregular Actuators	0.22
Voltage Step Size	0.18
Stability	0.12
Measurement Error	0.20
Total	0.56

to 0.54 nm rms over controllable spatial frequencies and identified the individual contributors to wavefront error in an error budget. The largest contributor is edge effects caused by scattered light interpreted as wavefront error by the PSDI. We have characterized the yield and actuator uniformity contributing to better calibration and providing feedback for device improvements. The most recent device has 99.5% normal actuators, which is a dramatic improvement over the early segmented device with 94.1% normal actuators[9]. In particular the most recent device has no dead actuators within an aperture 27 actuators across, greatly improving the performance. Overall the level of closed loop performance, without additional improvements, meets the precision and accuracy requirements for a high-contrast giant-planet imager and demonstrates the feasibility of MEMS technology for such an instrument.

### Acknowledgments

This work has been supported by the Gordon and Betty Moore Foundation through its grant to the UCO/Lick Observatory Laboratory for Adaptive Optics and the NSF Science and Technology Center for Adaptive Optics, managed by the University of California at Santa Cruz under cooperative agreement No. AST-9876783. This work was performed under the auspices of the U.S. Department of Energy by the University of California, Lawrence Livermore National Laboratory under contract No. W-7405-Eng-48.

\*Ph.D.candidate at University of California, Davis